Biosensors and Bioelectronics 267 (2025) 116786

Contents lists available at ScienceDirect

Biosensors and Bioelectronics

journal homepage: www.elsevier.com/locate/bios

Multi-functional, conformal systems with ultrathin crystalline-silicon-based bioelectronics for characterization of intraocular pressure and ocular surface temperature

Yuting Shao [a,b,h,1], Bofan Hu [c,1], Xin Liu [d,1], Zhuofan Ni [e,1], Yiyang Shu [a], Xiruo Zhang [a], Jiaqi Shen [a], Li Liang [e], Lianjie Zhou [b], Junhan Liu [c], Xiao Li [f], Juan Zhang [a], Lichao Ma [b], Zengfeng Di [g], Yongfeng Mei [b,c], Rui Li [e,*], Yanlong Bi [a,**], Enming Song [a,b,c,h,***]

[a] Department of Ophthalmology, Tongji Eye Institute, Tongji Hospital, School of Medicine, Tongji University, Shanghai, 200065, People's Republic of China
[b] Shanghai Frontiers Science Research Base of Intelligent Optoelectronics and Perception, Institute of Optoelectronics, Fudan University, Shanghai, 200438, People's Republic of China
[c] Department of Materials Science & State Key Laboratory of Molecular Engineering of Polymers, Fudan University, Shanghai, 200438, People's Republic of China
[d] Department of Ophthalmology, Guizhou Provincial People's Hospital, Guiyang, 550000, People's Republic of China
[e] School of Mechanics and Aerospace Engineering, State Key Laboratory of Structural Analysis, Optimization and CAE Software for Industrial Equipment, and International Research Center for Computational Mechanics, Dalian University of Technology, Dalian, 116024, People's Republic of China
[f] School of Biomedical Sciences, Heart and Vascular Institute and Li Ka Shing Institute of Health Science, Faculty of Medicine, The Chinese University of Hong Kong, People's Republic of China
[g] Shanghai Institute of Microsystem and Information Technology (CAS), Shanghai, 201800, People's Republic of China
[h] State Key Laboratory of Integrated Chips and Systems, Frontier Institute of Chip and System, Fudan University, Shanghai, 200438, People's Republic of China

ARTICLE INFO

Keywords:
Glaucoma
Bioelectronic
Multi-function
Intraocular pressure
Ocular surface temperature

ABSTRACT

Technologies that established *in vivo* evaluations of soft-tissue biomechanics and temperature are essential to biological research and clinical diagnostics, particularly for a wide range of eye-related diseases such as glaucoma. Of importance are advanced bioelectronic devices for high-precise monitoring of intraocular pressure (IOP) and various ocular temperatures, as clinically proven uses for glaucoma diagnosis. Existing characterization methods are temporary, single point, and lack microscale resolution, failing to measure continuous IOP fluctuation across the long-term period. Here, this work presents a multi-functional smart contact lens, capable of rapidly capturing IOP fluctuation and ocular surface temperature (OST) for assistance for clinical use. The microscale device design is programmable and determined by finite element analysis simulation, with detailed experiments of *ex vivo* porcine eyeballs. Such compact bioelectronics can provide high-precise measurement with sensitivity of 0.03% $mmHg^{-1}$ and 1.2 $\Omega\ ^{\circ}C^{-1}$ in the range of Δ2~50 mmHg and 30–50 °C, respectively. *In vivo* tests of bio-integration with a living rabbit can evaluate real-time IOP fluctuation and OST, as of biocompatibility assessments verified through cellular and animal experiments. The resultant bioelectronic devices for continuous precise characterization of living eyeballs can offer broad utility for hospital diagnosis of a wide range of eye-related disorders.

* Corresponding author.
** Corresponding author.
*** Corresponding author. Shanghai Frontiers Science Research Base of Intelligent Optoelectronics and Perception, Institute of Optoelectronics, Fudan University, Shanghai, 200438, People's Republic of China.
E-mail addresses: ruili@dlut.edu.cn (R. Li), biyanlong@tongji.edu.cn (Y. Bi), sem@fudan.edu.cn (E. Song).
[1] These authors contributed equally to this article.

https://doi.org/10.1016/j.bios.2024.116786
Received 27 March 2024; Received in revised form 28 May 2024; Accepted 15 September 2024
Available online 18 September 2024
0956-5663/© 2024 The Authors. Published by Elsevier B.V. This is an open access article under the CC BY-NC license (http://creativecommons.org/licenses/by-nc/4.0/).

1. Introduction

Continuous monitoring of biomechanics and temperature of soft biological tissues/organs has broad relevance in clinical diagnosis and treatment of diseases, particularly for a wide range of eye-related disorders. Glaucoma, a prevalent global cause of irreversible vision impairment, manifests as progressive optic neuropathies marked by the degeneration of retinal ganglion cells and subsequent alterations in the optical nerve head (Jayaram et al., 2023). Given the increasing population of elderly individuals, it is estimated to be ~111.8 million patients with glaucoma by the following 20 years (Tham et al., 2014). Such disease remains a complex multi-factorial disease, with its underlying mechanisms still not fully comprehended and difficult to diagnose (Weinreb et al., 2014). An important focus is on the intraocular pressure (IOP) that fluctuates between 10 and 21 mmHg in the normal state (Jayaram et al., 2023; Weinreb et al., 2014), resulting from the aqueous humor production, aqueous humor outflow, and episcleral venous pressure. As the basis for glaucoma evaluations, the pathophysiologic conditions can significantly raise the IOP fluctuation range (Sihota et al., 2018), simultaneously with the increase of ocular surface temperature (OST) as inflammation occurs (Leshno et al., 2022; Shen et al., 2022). Given that glaucoma is asymptomatic until advanced stages (*i.e.* visual impairments occur), of critical importance, is the demand for the early detection and real-time monitoring of abnormal IOP fluctuation and OST, serving as the key evidence for the assistance for clinical diagnosis (Medeiros et al., 2008; Shin et al., 2023).

Existing characterization methods of measuring IOP typically involve the use of tonometers, such as different tonometers, including various types such as Goldmann applanation, non-contact, rebound, and handheld tonometers. These techniques assess IOP by gauging the force necessary to flatten a specific corneal area, yielding limited numbers of measurements at specific time points during hospital healthcare, failing to track time-dependent changes at nocturnal periods during sleep state, when the highest level of IOP fluctuation for glaucoma patients occurs, usually outside of hospital and laboratory settings (Liu et al., 2003; Subramaniam et al., 2021). An alternative known as 24-h IOP monitoring provides quantitative measurements conducted at least six times within hours of an interval, as clinically proven to be inconvenient and fatiguing methods for hospital use.

Emerging classes of soft bio-integrated systems offer powerful options in this context, such as conformal implants in contact with the ocular surface for minimally invasive and biologically safe operation (Ray et al., 2019; Y. Zhu et al., 2022). Recent researches have established the use of thin, flexible piezoelectric sensors for the characterization of soft biomechanics of eyeballs, by virtue of measuring physical parameters such as tiny biological deformations and/or OST at superficial depth (Liu et al., 2024; Shi et al., 2021; Yang et al., 2021). Material approaches include metal, carbon nanotube/particles, and two-dimensional materials such as graphene, in micro/nanoscale designs (Fan et al., 2021; Liu et al., 2020; Pang et al., 2019; Xu et al., 2020). Although these candidates are of some interest, those that exploit well-established flexible inorganic semiconductors via transfer-printing technologies often provide superior levels of functionality, at performance levels approaching that of conventional wafer-based integrated circuits. The most recent study has demonstrated ultrathin strain gauges based on silicone nanomembrane (Si-NM), with designs that offer IOP monitoring for the ocular conditions of humans (Kim et al., 2021). Nevertheless, such a platform involves the use of a rigid, planar reinforced ring as substrates in contact with eyes for enhancement of measurement sensitivity (0.05% $mmHg^{-1}$), where their high modulus can lead to discomfort and particularly measurement uncertainty with an unstable biotic/abiotic interface during long-term use. Therefore, an important goal of these systems is the integration of compliant bioelectronics in tissue-compatible design that can fully bend, stretch, and twist in seamless contact with moving eyeball surfaces, to support stable, chronic measurements in a manner that can provide high levels of device performance, and superior bio-compatibility, ultimately for translation to human-eye healthcare.

This paper presents a flexible, bio-integrated system of the smart contact lens, referred to as *P&T@DG*, capable of rapidly and precisely capturing IOP fluctuation and monitoring OST, at a broad range of measurements, for assistance for multi-diagnosis of glaucoma. The device combines a uniquely designed IOP gauge based on Si-NR and OST sensor in optimal configurations on a molded contact lens, achieved through the finite element analysis simulation and basic experiments. The use of serpentine electrodes enhances the overall stretchability, while the seamless fit of the contact lens forms a long-term functional electrical interface targeting the ocular surface. The subsequent section details the performance testing of the IOP gauge on *ex vivo* porcine eyeballs within a specified range and rate of fluctuation, revealing the high sensitivity and linearity of the IOP gauge. The interaction between the IOP gauge and OST sensor has been specially studied and can be disregarded within a defined range. Furthermore, *in vivo* experimenting on animal models assesses the real-time IOP fluctuation and OST in live rabbits, followed by evaluations of bio-compatibility through both cell and animal studies. Such compact electronic devices designed for the rapid and precise characterization of living eyeballs have the potential to be valuable tools for diagnosing a variety of eye-related disorders such as glaucoma.

2. Experimental

2.1. Fabrication of the IOP gauge and temperature sensor

The process was initiated by the highly p-doping process on a silicone-on-insulator (SOI) wafer (Soitec Inc.). Boron was pre-deposited in a furnace at a temperature of 1100 °C for 35 min in a flow of N_2 (1000 standard cm^3 min^{-1}) using the rapid thermal annealing process to diffuse boron uniformly across the 500-nm-thick top Si layer. After patterning the Si layer with micro-holes (4 μm diameter) using reactive ion etching (RIE), the silicone nanomembrane (Si-NM) was transferred onto a target substrate of polyimide (PI, 2 μm thick) by etching away the buried oxide layer of the SOI wafer using a 40% HF solution (~30 min) and picking up the Si-NM using a polydimethylsiloxane (PDMS, Sylgard 184, Dow corning) stamp (4:1) (Fig. S1a). After this transfer process, the specialized Si-NM pattern of the IOP gauge was defined using RIE and turned into silicone nanoribbon (Si-NR). Then serpentine electrodes (Cr/Au, 10/200 nm thick) of the IOP gauge and temperature sensor were deposited using sputtering and patterned photolithographically (Fig. S1b). After fabricating the fully integrated circuit on the glass substrate, the samples were coated with a layer of silicon dioxide (SiO_2) (70 nm thick) and then transferred onto both planar and spherical substrates to go further test using water-assisted transfer printing method (Lee et al., 2011) in Fig. S1c. In the process of the transfer, the devices do not produce wrinkles after carefully printing onto the receiving surface (i.e. planar or spherical surfaces), as we will detailed later.

2.2. FEA

To determine the optimal sensing position of the cornea map for the IOP gauge, we used FEA (Abaqus/CAE, 2021 version) to simulate the strain and displacement of the human cornea in horizontal and vertical axes under varying IOP levels. We also simulated the strain that occurs when the device is subjected to IOP fluctuation at Δ1, 10, and 50 mmHg. The parameters of the eye and contact lens for FEA are listed in Table S1.

2.3. Characterization

The morphology and structure of Si-NR were characterized by scanning transmission electron microscopy (SEM, Zeiss Sigma 300) and Raman spectroscopy (inVia Qontor). The thickness of Si-NR was

performed by a profilometer (Dektak XT). The electrical characteristics of the IOP gauge and OST sensor were determined using a probe station (Keithley 4200-SCS).

2.4. Optimal test of the IOP gauge and performance

To determine the most suitable material and pattern for preparing the IOP gauge, we transferred three sets of strain gauges (Si_l group: K = 0.22 mm^{-1}, Si_s group: K = 3.85 mm^{-1}, and Au_s group: K = 3.85 mm^{-1}) to a planar PDMS substrate (ratio: 10:1, 2 mm thick). Silver wire (Kesirui New Material Ltd.) and silver conductive paint (05001-AB, SPI) were used to extend the electrodes and fix them to the crocodile clamp of the electrochemical workstation (ECW, CHI660E, CH Instruments Inc.). The results of three gauges stretching at different applied strains (1, 3, 5, and 7%) on the X-axis using the stretch meter (57H56SS, DYCH Company) were recorded in ECW (Fig. S2a). According to the recorded data, we calculated and compared the gauge factor (GF) of the three kinds of gauges. Each group had three representative devices and performed at least nine experiments. $GF=(\Delta R/R_0)/\varepsilon$, where ΔR, R_0, and ε are the variation of the electrical resistance, initial electrical resistance, and the applied strain of the gauge, respectively (Yang and Lu, 2013). The set of gauges with the largest GF value was used to complete the mechanical performance characterization. The working interval of ECW was set as 0.02 s in *i-t* mode and the working voltage is 1 V.

2.5. Optimal test of the OST sensor

To determine the optimal design for the OST sensor of the *P&T@DG*, we designed three patterns as shown in Fig. 2h. We set up a test platform that includes hot plates, thermometer (UT325, LINI-T), and ECW to be tested (seen in Fig. S2b). The thermometer was used for hot plate temperature calibration. The temperature range was adjustable from 30 to 50 °C. The ECW recorded the change in the electrical resistance value of the device as the temperature increased or decreased. The sensitivity (SE) of the OST sensor was calculated as the formula of SE = $\Delta R/T$, where ΔR and T denote the variation of electrical resistance and the sensing temperature. Three samples were tested per group, and each sample was tested at least three times. The experiment was conducted at

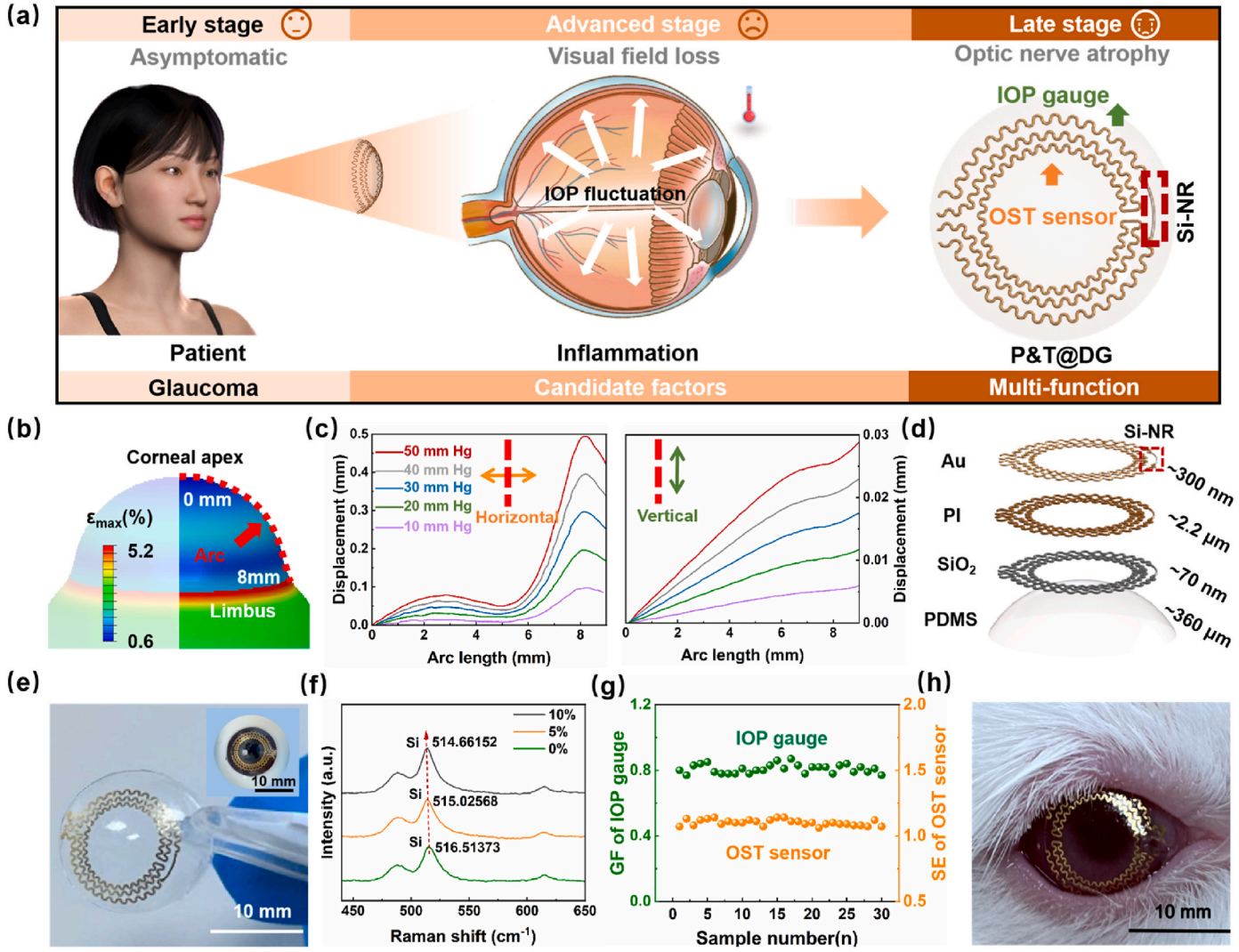

Fig. 1. Illustration of characteristics of Glaucoma and multi-functional smart contact lens named P&T@DG. (a) The characteristics of Glaucoma in three stages and the top view of the device named *P&T@DG*. The red dotted line demonstrates Si-NR. (b) The strain map of the eyeball under 10 mmHg. (c) Finite element analysis (FEA) of an arc (red dotted line) on the cornea under varying levels of IOP (ranging from 10 to 50 mmHg) along the horizontal and vertical axes. (d) The stacked diagram of the P&T@DG. (e) The photograph of a device held by a clamp. Inset is a photograph of a device on an artificial eye. (f) The substance distribution of the strain gauge under the applied strain of 0, 5, 10% during Raman spectroscopy test. The red dotted arrow indicates the shift of Si peak. (g) Gauge factor (GF) of IOP gauges (green) and sensitivity (SE) of OST sensors (orange) among 30 prepared devices. (h) The photograph of a device on a rabbit eyeball. IOP: intraocular pressure; OST: ocular surface temperature; Si-NR: silicone nanoribbon; PI: polyimide; SiO_2: silicon dioxide; PDMS: polydimethylsiloxane. GF: gauge factor; SE: sensitivity.

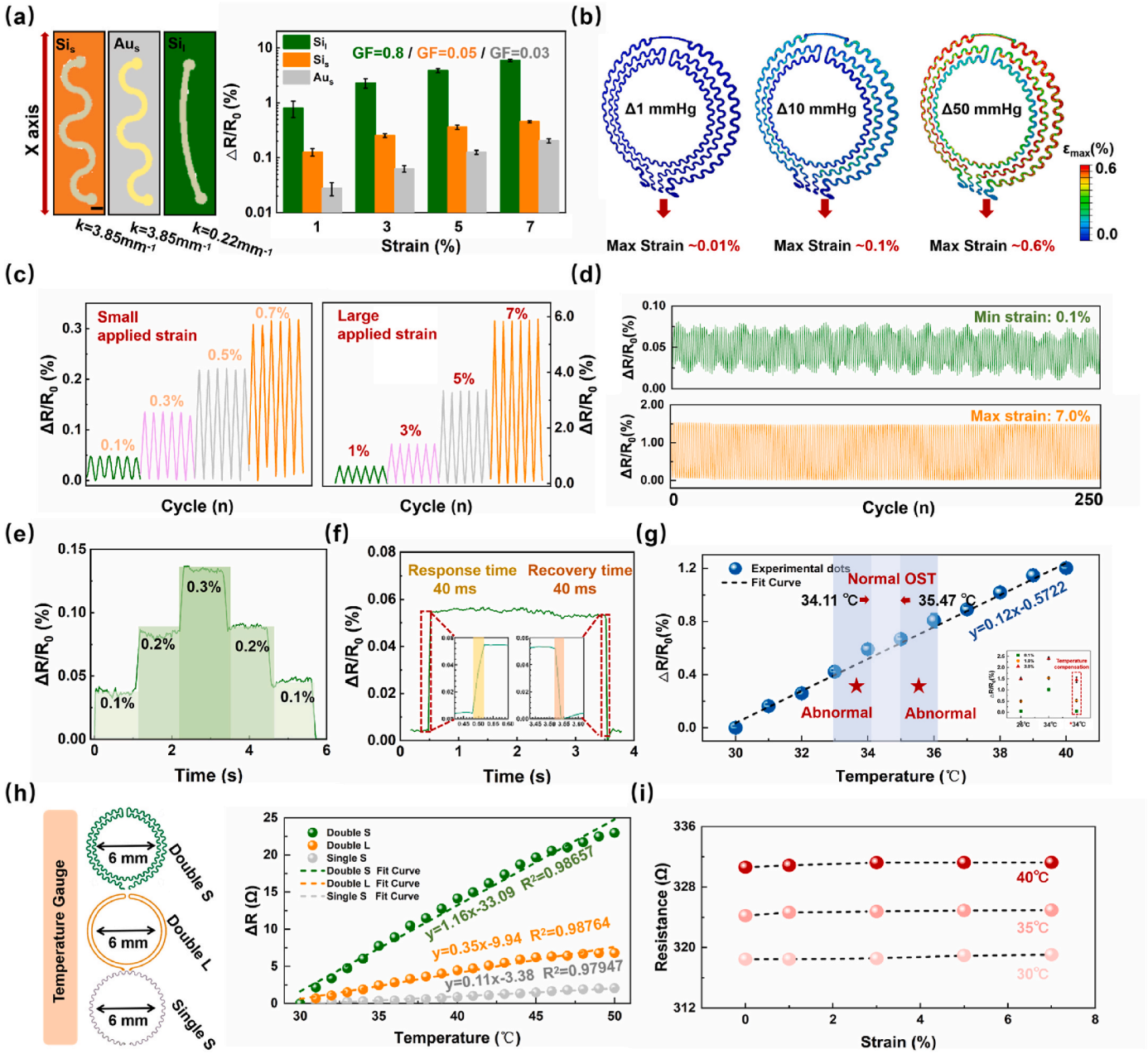

Fig. 2. Optimization experiments and basic performance characteristics of the IOP gauge and OST sensor. (a) The relative electrical resistance change rate and fit curve among the Si_s group (orange, k = 3.85 mm^{-1}), Au group (gray, k = 3.85 mm^{-1}), and Si_l group (green, k = 0.22 mm^{-1}) under applied strain of 1, 3, 5, 7% in X axis stretching test. The relative electrical resistance change rate values are log-transformed for analysis (log10). Error bars correspond to the standard deviation for nine measurements with three representative devices. (b) Simulation (FEA) results of Si-NR in Si_l-Au configuration for internal strain as a function with varying IOP levels of Δ1, 10, 50 mmHg. (c) The relative electrical resistance change rate of a representative device in the Si_l group after applying the small strain of 0.1, 0.3, 0.5, 0.7% and large strain of 1, 3, 5, 7% for each of five cycles. (d) The results of a representative device in the Si_l group under 250 cyclic with the applied minimum strain of 0.1% and maximum strain of 7%. (e) The step response performance of a representative device in the Si_l group. (f) The response and recovery time of a representative device in the Si_l group under operation. (g) Influence of temperature from 30 to 40 °C on the sensing performance of the IOP gauge. Inset indicates the calibration of the temperature compensation on the device upon the temperature shift from 26 to 34 °C under the applied strain of 0.1, 1, and 3%. Error bars correspond to the standard deviation for nine measurements with three representative devices. (h) The resistance change and fit curve of three patterns of the temperature gauges (Double S, Double L, and Single S) within a range of 30~50 °C. (i) Influence of applied strain of 1, 3, 5, and 7% on the sensing temperature (30, 35, and 40 °C) of a representative device in the Double S group. GF: gauge factor; OST: ocular surface temperature.

a standard controlled indoor temperature of 26 °C.

2.6. Porcine eyeball experiment

The optimal strain gauge was selected for the preparation of the IOP gauge. Fresh porcine eyeballs were prepared from the slaughterhouse within 4 h. The *ex vivo* test platform is demonstrated in Fig. 3a and b. The rate and amplitude of IOP fluctuation were regulated by the velocity and volume of fluid entering and exiting the anterior chamber. The fluid was controlled by a micro-injection pump (Harvard Apparatus), which connected a tube with a scalp needle inserting the anterior chamber of the eye. The IOP inside the eyeball was calibrated by a commercial manometer (Testo 510i) connecting with another scalp needle inserting the anterior chamber. Commercial manometer measured at 1-s interval.

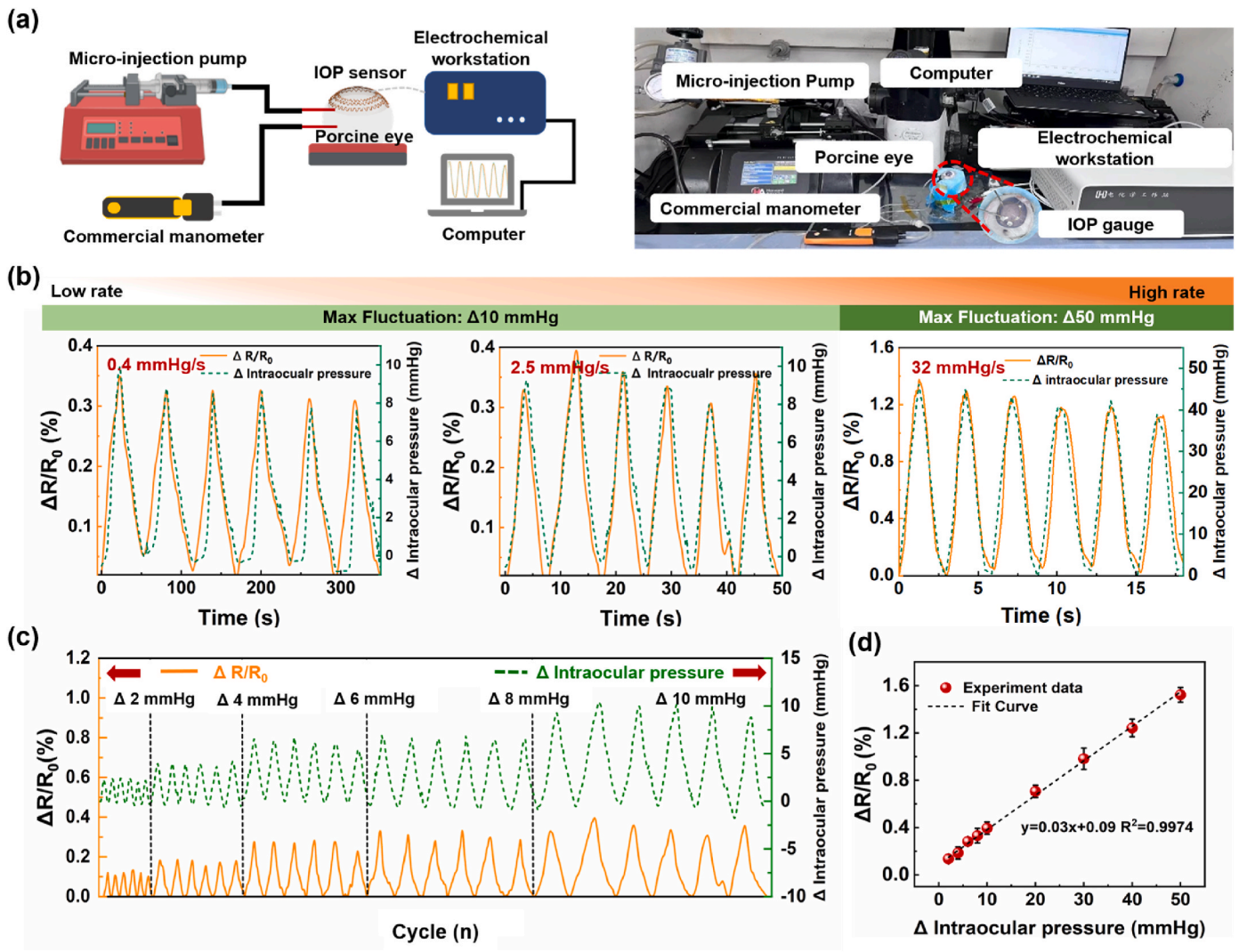

Fig. 3. Application of the IOP gauge in porcine eyeballs *ex vivo*. (a) The sketch (left) and photograph (right) of the setup of the IOP test in porcine eyeballs. (b) The relative electrical resistance change rate and change of IOP level followed 5 cycles of max fluctuation at Δ10 and 50 mmHg, with varying rates of IOP fluctuation at 0.4, 2.5, 32 mmHg s^{-1}, using an IOP gauge (orange line) and a commercial manometer (green dotted line). (c) The results of the IOP gauge and the commercial manometer with IOP fluctuation of Δ2, 4, 6, 8, and 10 mmHg, each for five cycles. (d) The experimental values (red dots) and fit curve (black dotted line) of the IOP gauge in the range of Δ2 to 50 mmHg. Error bars correspond to the standard deviation for nine measurements with three representative devices. IOP: intraocular pressure.

Changes in the electrical resistance rate of IOP gauges were calculated from the data of the ECW. The working parameters were the same as above. Each of the experiments was performed at least three times.

2.7. Rabbit experiment

All *in vivo* animal experiments were approved by the Ethics Committee of Tongji Hospital Affiliated with Tongji University, approval number (2021-DW-005) and conducted at a standard controlled indoor temperature of 26 °C. We used *P&T@DG* to record IOP and OST in anesthetized rabbits' eyes for 30 min. In the experiment, female New Zealand rabbits larger than 2.5 kg were selected, and 3% sodium pentobarbital was used for intraperitoneal anesthesia (30 mg kg^{-1}). During the work, the anesthetic should be continuously supplemented to avoid the rabbit awakening and affecting the recording. We simulated IOP fluctuation by constructing a platform as mentioned above, replacing the micro syringe pump with a manually controlled syringe, including three clinical situations, namely normal IOP fluctuation, acute elevation of IOP (i.e. acute angle closure glaucoma attack), and sudden drop of high IOP (i.e. paracentesis of anterior chamber). All these clinical manifestations are common in clinical practice but have not been recorded in detail over time.

The left eye of the rabbit was used as the experimental eye with the eyelid opener opening the eyelid. The baseline IOP and OST values of the eye were first obtained using the handheld tonometer (SW-500) and thermal imager (Seek Thermal) according to the clinical practice principle. The *P&T@DG* was worn on the left eye and linked to the two ECWs to record the two kinds of values, respectively. The parameters of ECWs were set as a 1-min interval and run time of 30 min. The handheld tonometer and thermal imager were measured and recorded at once every 5 min. To facilitate the measurement of the handheld tonometer in the same eye, we cut off a circular area with a radius of about 2 mm in the central part of the smart contact lens, so that the measurement needle of the handheld tonometer can be in direct contact with the cornea to obtain accurate reference IOP values. Output values of the ECWs were recorded and converted into IOP and OST values through the formula with given reference values by Excel software. These data were compared with the data recorded from a handheld tonometer and thermal imager.

The thermal imager was also used to detect the heating of the device

after 30 min of wearing. After 24 h of wearing the device, the conjunctival sac was stained with fluorescein sodium test strips, and healthy states of the ocular surface were assessed and photographed using cobalt blue light. Under the light, yellow areas indicate epithelial damage.

2.8. Cell viability experiment

The ethylene oxide sterilized device was placed into the prepared cell culture medium mixed with 10% fetal bovine serum (CellCook cat: CM1002L) and complete medium (DMEM/F12, GIBCO CAT: 11330) to obtain a 24-h leaching solution.

Murine corneal epithelial cells (Icell Bioscience Inc, Shanghai, China) were cultured with the leaching solution and normal culture medium, respectively. Cells were cultured in a humidified incubator at 37 °C with 5% CO_2. After 1 and 3 days of culture, cell viability was assessed using the Calcein-AM/PI Double Stain kit (Yeasen, 40747ES76). The red cells signified deceased cells, while green cells indicated living cells. Cell viability was calculated as the percentage of green cells divided by the total number of cells, multiplied by 100%. The experiment was conducted a minimum of three times for accuracy (Guo et al., 2021).

Cell Counting kit-8 (CCK-8) was also carried out to examine cell viability. At the end of the 24 h and 72 h, the absorbance (O.D.) values at a wavelength of 450 nm were tested, respectively. The magnitude of absorbance values reflected the number of living cells (Ye et al., 2022). The experiment was performed at least three times.

3. Results and discussion

3.1. Structural design, performance characteristic, and fabrication of the P&T@DG

Sensors specifically tailored to the unique characteristics of various eye diseases are of particular interest, because these techniques can integrate with soft contact lenses to efficiently transmit a range of physiological and biochemical information from the cornea through direct contact. Information of significance may include IOP, OST, ion concentration, glucose levels, and other relevant metrics, which can be utilized for diagnostic and therapeutic purposes (Y. Zhu et al., 2022). Fig. 1a illustrates the characteristics of glaucoma alongside the top view of our device. Patients with glaucoma typically exhibit early asymptomatic signs, followed by progressive loss of visual field and optic nerve atrophy in the advanced to late stages. The majority of patients have already progressed to the latter two stages upon diagnosis. The conventional approach to early detection involves tonometer measurements of IOP at a single time point, which have been associated with a notably high rate of missed diagnosis (Tham et al., 2014). Further investigation is required using advanced bioelectronic devices. IOP fluctuation and inflammation are proposed candidate factors in current clinical research for glaucoma (Baudouin et al., 2021; Medeiros et al., 2008; Shin et al., 2023). The increase in temperature is recognized as a consequence of systemic inflammation, thus the detection of OST can serve as an assessment of inflammatory conditions and aid in the diagnosis of glaucoma (Leshno et al., 2022; Shen et al., 2022). An important feature of this work is the integration of a contact lens with multi-functional sensors, focusing on candidate factors related to IOP fluctuation and OST elevation (inflammation) in individuals with glaucoma. The outer circle of the device represents an IOP gauge, which comprises a strain gauge of Si-NR, while the inner circle denotes an OST sensor. Together, these components comprise a multi-functional smart contact lens, which refers to *P&T@DG*. It is anticipated for use in the early stage of glaucoma patients presenting asymptomatic to reduce missed diagnoses during glaucoma screening.

Assuming that the deformation in the strain gauge aligns with that of the cornea, we have mathematically established a proportional relationship between the change in relative electrical resistances and IOP levels (Fig. S3), which laid the foundation for measuring IOP fluctuation using piezoresistive-based devices. The strain gauge within the *P&T @ DG* necessitates careful consideration of its placement on the cornea in accordance with corneal deformation. Fig. 1b and c shows the utilization of FEA modeling to determine the strain and displacement of the eyeball under varying levels of IOP (ranging from 10 to 50 mmHg). The strain map of the eyeball under 10 mmHg is demonstrated as an example in Fig. 1b. The displacement of a representative arc (red dotted line), measuring from the corneal apex (0 mm) to the limbus (8 mm), which refers to the junction between the cornea and conjunctiva, along the horizontal and vertical axes is calculated from the FEA modeling. The findings indicate a positive correlation between IOP and displacement in both axes. Additionally, at equivalent IOP, the displacement along the horizontal axis surpasses that along the vertical axis, reaching its maximum at the 8 mm region proximal to the limbus. The above results suggest that the strain gauge should be arranged along the horizontal axis and close to the limbus, consistent with results in previous research (Dou et al., 2021).

Fig. 1d presents the stacked diagram of the device, where a bottom layer in the form of a PDMS contact lens (360 μm thick), serving as soft contact with the ocular surface. A top layer of PI (2 μm thick) encapsulates multi-functional devices of IOP gauge and OST sensor. Among this, the IOP gauge consists of a lithography-defined ultrathin Si-NR (300 nm thick) while the OST sensor comprises thin-film electrodes of gold (Au) in serpentine design (200 nm thick), both with metal interconnection. The total thickness of the electronic platform is ~360 μm, with an area of 10 mm × 10 mm. Device fabrication starts with solid-state phosphorus doping (1100 °C for 35 min) of p-type device Si on a SOI wafer (top layer 500 nm thick) with a concentration of 1020 atoms per cubic centimeter, followed by transfer printing metal onto a PI film on a temporary glass substrate. The sequence of lithography, etch, and metal connection yields the multi-functional device platform, subsequently transferred onto the PDMS substrate that serves as a mechanical interface with the ocular surface. The detailed procedure is described in the methods and Fig. S1. Fig. 1e shows the completed preparation of *P&T@DG*, with the inset depicting an optical image of an artificial eyeball wearing a *P&T@DG*. As for the working principle of the strain gauge, Fig. 1f shows the Raman spectroscopy test of the monocrystalline Si-NR in ultrathin structure under different strain levels of 0, 5, and 10%. The Raman peak shifts from 516.51 to 514.66 cm^{-1} under different strain levels above, results of which indicate the increasing applied strain within materials can lead to a left shift of the Raman peak of silicon. Thus, the piezoresistive effect of Si-NR is potentially attributed to alterations in lattice parameters caused by the applied strain, which subsequently affects the band structure of the Si-NR and can result in variations in carrier mobility (Kanda, 1991; Yang and Lu, 2013).

For the device characteristics, Fig. 1g summarizes statistical results for GF of the IOP gauge and SE of the OST sensor, measured from 30 variable *P&T@DG*. The results suggest excellent uniformity and consistency in the device performance across the fabricated systems, with an average value of GF of the IOP gauge is 0.81 ± 0.03 and the sensitivity of the OST sensor is 1.20 ± 0.02 Ω $°C^{-1}$, respectively, with the electrical resistance of the IOP gauge being 2147.0 ± 203.3 Ω and that of the OST sensor 314.4 ± 13.14 Ω (Fig. S4). Other characteristics of Si-NR are in Fig. S5. As a consequence, the multi-functional device can offer potential clinical significance in rapidly identifying eye-related disorders such as glaucoma and inflammation, with quantitative metrics that have promise as diagnostic biomarkers for biological targets of animal models and human subjects, as shown in Fig. 1h.

3.2. Optimization experiments and basic performance characteristics of the IOP gauge and OST sensor

Beyond the excellent piezoresistive properties of Si-NR with high GF, the utilization of optimal materials and pattern design for the strain

gauges can also enhance the sensitivity of IOP gauges. Fig. 2a illustrates the relative electrical resistance change rate and related fit curves of different materials and patterns, with three groups (Si_s group, k = 3.85 mm^{-1}; Au_s group, k = 3.85 mm^{-1}; and Si_l group, k = 0.22 mm^{-1}) under the applied strain of 1, 3, 5, 7% in X axis (red double-arrow) stretching test. The GF is employed to quantify the mechanical sensitivity of the device as explained above. Results of the serpentine-shaped gauges with different materials indicate that the GF value of the Si_s group is 0.05, surpassing that of 0.03 of the Au_s group. Furthermore, the curvature of the Si-NR in a linear-shaped design (Si_l group, right of Fig. 2a) can offer the highest GF of 0.8 in all three groups. These findings align with the outcomes reported in previous work, indicating that under the same stretching, the greater the curvature of the Si-NR, the smaller the GF value of the device (Kim et al., 2014). As such, we exploit the design of the Si_l group as a functional gauge device, to yield components with capabilities in measuring IOP across eyeballs with high GF and sensitivity. Increasing the length of the Si-NR has also been proved to increase sensitivity using FEA in Fig. S6, with a length of 1.5 times the original version in a larger strain distribution across the device area (0.2%) and the Si-NR (0.06%) than the original version (0.1%; 0.05%). However, it poses a challenge to the transfer printing process and thus limit the device yield for fabrication. Previous reports on the size of Si-NR are mostly within 200 μm in length (Son et al., 2014; Kim et al., 2014, 2021), lower by an order of magnitudes than the length of our version of 2.89 mm. In this context, Fig. 2b depicts the simulated strain generated by an IOP gauge in the Si_l-Au configuration under varying IOP levels of Δ1, 10, and 50 mmHg. The results show that the maximum strain values are 0.01, 0.1, and 0.6% at Δ1, 10, and 50 mmHg, respectively, which are well within the measurement range of Si-NR in linear-shaped structure and similar to the previous research (Kim et al., 2014). Although the Au trace has a greater strain than Si-NR in Fig. 2b, the electrical resistance change of Au trace under the same tensile strain is around 0.1% of that of Si-NR, and the electrical resistance change rate is much smaller than that of the Si-NR (0.15% vs 5%). Therefore, the response of the device is mainly attributed to the Si-NR, with more details in Fig. S7.

The mechanical performances in linear-shaped design (Si_l group) are further characterized in Fig. 2c–g. It can effectively record the relative electrical resistance change rate after applying the external force, under strain not only in a small range (0.1, 0.3, 0.5, and 0.7%) but also in relatively high level (1, 3, 5, and 7%), respectively, as shown in Fig. 2c. In all cases, the device displays high-precision measurement during tensile test, with a trend consistent with corresponding levels of IOP fluctuation that ranges from Δ1 to 50 mmHg. Fig. 2d presents the results of a representative device in the Si_l group under almost 300 cyclic tests with a minimal strain of 0.1% and a maximal strain of 7.0%. The results demonstrate the commendable stability and repeatability of the candidate IOP gauge. Additionally, Fig. 2e showcases the step response performance. By subjecting the gauge to strain increments of 0.1% every second up to 0.3%, followed by corresponding decrements back to the initial state, the device demonstrates favorable dynamic mechanical responsiveness. Analysis in Fig. 2f indicates a rapid response time of 40 ms and a recovery time of 40 ms, which can establish a foundation for prompt reactions to IOP fluctuation. To exclude other external influences on the functional device, Fig. 2g illustrates the proportional rate of change in electrical resistance of a typical IOP gauge in the Si_l group as the external temperature rises from 30 to 40 °C. The finding indicates that with each 1 °C rise in temperature, the relative electrical resistance change rate of the IOP gauge is only ~0.1%, compatible with the magnitudes of $\Delta R/R_0$ induced by increasing 0.1% strain. The inset of Fig. 2g displays the measured values and temperature-compensated corrected values (red dotted square) of the relative electrical resistance change rate under applied strains of 0.1, 1, and 3% as the temperature ranges from 26 to 34 °C. Glaucoma patients generally suffer an elevated temperature of 0.9 ± 0.3 °C across ocular surfaces compared to that of healthy states (Leshno et al., 2022), where these changes of temperature can be negligible as contribution to IOP gauge measurements, particularly within the IOP fluctuation range from Δ8 to 50 mmHg that is mostly associated to reported glaucoma patients (Lee et al., 2010; Leidl et al., 2014; Medeiros et al., 2008; Shin et al., 2023). Therefore, it is worth noting that in the temperature variation range of clinical scenarios, especially within the normal (red arrows) and abnormal states (red stars), the values are less affected.

In addition to IOP fluctuation, the elevated OST of the multifunctional device is also essential to precisely detect inflammation for the pathophysiology of glaucoma. However, in certain specific circumstances, the measurement of OST using conventional thermal imagers becomes challenging. Consequently, monitoring OST using contact lenses could serve as a crucial form for diagnosing glaucoma and assessing the efficacy of treatment, thereby playing a complementary role to the IOP gauge for hospital diagnosis. Similar to Fig. 2a, the OST sensor utilizes a thin gold and evaluates three groups of distinct patterns, specifically Double S, Double L, and Single S, as shown in Fig. 2h, where the inner diameter should be at least 6 mm to ensure transparency in the visual axis area. A comparative analysis of the sensitivity among the three groups, utilizing a designated testing platform (Fig. S2), was conducted within a range of 30~50 °C, as the OST of the healthy states ranging from 34.11 to 35.47 °C (L. J.H. Tan et al., 2009). Specifically, the Double S group exhibited the highest temperature measurement sensitivity at 1.16 Ω $°C^{-1}$, followed by the Double L group of 0.35 Ω $°C^{-1}$ and the Single S group of 0.11 Ω $°C^{-1}$. Recent work has established gold film to fabricate the OST sensor, achieving a sensitivity of 0.94 Ω $°C^{-1}$ (also within the temperature range from 30 to 50 °C) (Guo et al., 2021), which is well consistent with our research results. Similarly, Fig. 2i shows the electrical resistance value of the OST sensor in the design of Double S following the application of strain of 1, 3, 5, and 7% at different temperatures (30, 35, 40 °C), respectively. The research results show that the effect of applied strain under various levels that is associated with glaucoma models on the OST sensor can be negligible. It is worth noting that the higher environmental temperatures lead to the initial higher electrical resistance of the Au-based OST sensor and does affect the OST (J.H. L. Tan et al., 2009), but it has little effect on the performance of the device with a stable sensitivity around 1.2 Ω per °C (Fig. S8), as we carefully control the indoor temperature as 26 °C and test after the device and OST is adapted in the experiments. Therefore, the impact of external temperature changes on the measurement of OST can be reduced.

3.3. Application of IOP gauge in porcine eyeball for ex vivo test

Ex vivo measurements for animal models involve IOP gauges with intimate contact of spherical substrate on the cornea of porcine eyeballs, under constant room temperature. Compared with the planar substrate, the spherical substrate of the contact lens hardly affects the morphology and electrical characteristics of the devices, as detailed in Fig. S9. Previous studies have reported that the anatomy of porcine eyeballs is similar to that of human eyeballs, especially the characteristics of thick central cornea and thin limbus, making it a standard animal model for biomechanical research (Leonardi et al., 2009; Liu et al., 2020; Nambiar et al., 2022; Shih et al., 2024). Fig. 3a illustrates the schematic illustration and photograph of the measurement platform with the application of the device on a porcine eyeball. The experimental setup is detailed in the methodology section. Subsequent tests select a voltage of 1 V in a safe fashion. During the measurements, IOP fluctuation tested on such porcine eyeballs can establish a long-term functional electrical interface that enables real-time monitoring of mechanical properties of tissues and thus serves as the diagnosis and prognosis for eye-related disorders such as glaucoma. However, the limited availability of clinical equipment capable of continuously monitoring tiny fluctuation of IOP poses a constraint on conducting more extensive clinical investigations (Leidl et al., 2014; Turner et al., 2019; Vitish-Sharma et al., 2018). Here, the design and function test of our IOP gauges aim to make up for the shortcomings of current devices.

Fig. 3b displays the relative electrical resistance change rate, with various levels of IOP fluctuation ranging from Δ10 to 50 mmHg, all using an IOP gauge (orange line) and a commercial manometer (green dotted line), respectively. Here, variable rates of IOP fluctuation are also tested at 0.4 mmHg s^{-1}, 2.5 mmHg s^{-1}, and 32 mmHg s^{-1}, where the data collected via the IOP gauge and commercial manometer vary consistently with different IOP fluctuation. Furthermore, Fig. 3c showcases the results of the IOP gauge and the commercial manometer with smaller IOP fluctuation of Δ2, 4, 6, 8, and 10 mmHg (each for five cycles), respectively. The results demonstrate the outstanding measurement capabilities for continuous monitoring of IOP for *ex vivo* animal model tests, where the IOP gauge is capable of detecting a minimal change as small as 2 mmHg with high measurement repeatability and operation stability. As a consequence, Fig. 3d illustrates the experimental values of the IOP gauge in the range of Δ2 to 50 mmHg, the results of which demonstrate a high linearity of 0.9974 and high measurement sensitivity as 0.03% $mmHg^{-1}$.

The IOP gauge with Si-NR in our case, based on the piezoresistive mechanism, shows excellent sensitivity, biocompatible, and conformal properties, resulting in accuracy, safety, and a wide range of IOP detection. Compared with LCR-based IOP contact lenses (Kim et al., 2017; M Kouhani et al., 2020; Yang et al., 2022; Yang H et al., 2024; H. Zhu et al., 2022), especially the capacitance type (Yang H et al., 2024), our platform is characterized by a simple structure, convenient data output, and a thin contact interface with the ocular surface, which improves both sensitivity and comfort to a large extent. For capacitance-based LCR circuits, the changes of resonant frequency depend on the changes of the dielectric layer thickness. It shows the advantages of wireless and low power consumption. More comparisons with other types of advantages are described in detail in Table S2. By comparison to other piezoresistive-type IOP gauges presented in Table 1, our study herein shows a notable advantage in high precision recording and measurement sensitivity (0.03% $mmHg^{-1}$). Similarly, the most recent work has established a high sensitivity of 0.05% $mmHg^{-1}$ via Si-NR-based device designs with ultrathin structure (single crystalline Si layer of 300 nm thick) that employs a reinforcing technique that includes high-modulus materials of resin to concentrate corneal strain in the specific region across ocular surfaces to measure localized IOP. Although promising, the stiff, planar, and rigid materials used for these systems are, however, fundamentally mismatched with the soft surfaces of the eyeball, which can cause discomfort to the wearer and induce invasiveness for chronic use (Kim et al., 2021). As a comparison, the *P&T@DG* system presented in this work is a fully conformal design that incorporates a soft substrate of PDMS materials in contact with curved, dynamic ocular surfaces, with great potential for non-invasive use for long-term monitoring.

Table 1
Comparison of the IOP gauges among the studies reported in recent years.

Reference	Material of strain gauge	Model	Sensitivity	Conversion	Range
Leonardi et al. (2009)	170 nm Pt and 25 nm Ti	Porcine eyeball	113 μV $mmHg^{-1}$	–	11–30 mmHg
Pang et al. (2019)	50 nm Pt and 10 nm Ti	Silicone eyeball	20 μV $mmHg^{-1}$ (I_0 = 100 μA)	0.20 Ω$mmHg^{-1}$	9–30 mmHg
Liu et al. (2020)	Graphene nanowalls	Porcine eyeball	42250 ppm $mmHg^{-1}$	4.225% $mmHg^{-1}$	0–75 mmHg
Xu et al. (2020)	Graphene	Silicone eyeball	150 μV $mmHg^{-1}$ (I_0 = 1000 μA)	0.15 Ω$mmHg^{-1}$	8–34 mmHg
Fan et al. (2021)	Graphene and carbon nanotubes	PDMS eyeball	36.01 μV $mmHg^{-1}$ (I_0 = 1000 mA)	0.000036 Ω$mmHg^{-1}$	9–34 mmHg
Kim et al. (2021)	Si NM/Si NR (~300 nm)	Bovine eyeball	0.05% $mmHg^{-1}$	–	4–20 mmHg
★ This work	Si NM/Si NR (~300 nm)	Porcine eyeball	0.03% $mmHg^{-1}$	0.60 Ω$mmHg^{-1}$	10–60 mmHg

3.4. Application of P&T@DG in rabbit eyes in vivo and cell compatibility

The *P&T@DG* can characterize the mechanical properties of a range of eye regions both *ex vivo* and *in vivo*. Results obtained from live rabbits with eye-related diseases in simulated clinical settings appear in Fig. 4. The sketch of the experimental platform and measurement time points is shown in Fig. 4a and b. Anesthesia status can affect normal IOP. For example, the use of phenobarbital and chloral hydrate anesthesia in mice can reduce IOP by approximately 5–8 mmHg within the initial 5 min (Qiu et al., 2014). Long-term, deep anesthesia can increase the mortality rate of experimental animals, mainly caused by low blood pressure and malfunction of temperature regulation (Alstrup et al., 2023). Therefore, we here exploit animal models of rabbits under anesthesia state within 30 min of every situation, to simulate different IOP fluctuation, where the *P&T@DG* can capture the key parameters across continuous experimental recording periods. In parallel, commercial tools that include the handheld tonometer and thermal imager can simultaneously monitor the IOP and OST, as a comparison to those obtained via *P&T@DG* (Fig. 4b). SW-500 as a handheld tonometer used in the experiment, is intended for humans, while TonoVet Plus is reported to be most suitable for rabbits (Gloe et al., 2019). We found that the values of SW-500 are slightly lower than those of TonoVet Plus in the IOP measurement of rabbits, as detailed in Fig. S10. Nevertheless, we pay more attention to IOP fluctuation instead of the exact value of IOP. Even if the calibration of the initial value varies, it hardly affects the observation of the result. Besides, other tonometers, intended for human and other animal species, are also applied for IOP calibration in living rabbits (Kim et al., 2021; Yang et al., 2022; Ye et al., 2022), as shown in Table S3. Further research on the selection of tonometers needs to be deployed for accurate measurement rather than trend calibration.

Fig. 4c shows an optical photograph of a living rabbit wearing the *P&T@DG* as a contact lens, with good light transmittance over 80% through a UV–vis spectrophotometer, determined by dividing the overall light transmittance value of the contact lens by the overall light transmittance value without specimens (Fig. S11).

A formula automatically calculates the device's output values into the IOP and OST values. For the OST calculation, the initial OST value is recorded as T_0 using a thermal imager, with the initial stable current reading as I_0 in the OST sensor of the *P&T@DG*. The current reading at any given time point is denoted as I_t. Based on the sensitivity of Fig. 2h, which is 1.16 Ω °C^{-1}, the OST value at any given time point, T_t, is calculated as $T_t = T_0 + [(-1)/I_t - (-1)/I_0]/1.16$, that is:

$$T_t = T_0 + \frac{I_t - I_0}{I_t I_0} \times \frac{25}{29}$$

For the IOP calculation: the initial IOP value is recorded as P_0 using a handheld tonometer, with the initial stable current reading as I_0 in the IOP gauge of the *P&T@DG*. The current reading at any given time point is denoted as I_t. Based on the sensitivity of Fig. 3d, which is 0.03% $mmHg^{-1}$, the IOP at any given time point, P_t, is calculated as $P_t = P_0 + [(-1)/I_t - (-1)/I_0]/(-1)/I_0/0.03\%$, that is:

$$P_t = P_0 + \frac{I_0 - I_t}{I_t} \times \frac{10000}{3}$$

The value from the OST sensor can also be used to calibrate the temperature shift of the IOP gauge in case the temperature change in a relatively broad range according to Fig. 2g. Within the IOP control system, a manually operated syringe is linked to a scalp needle that is

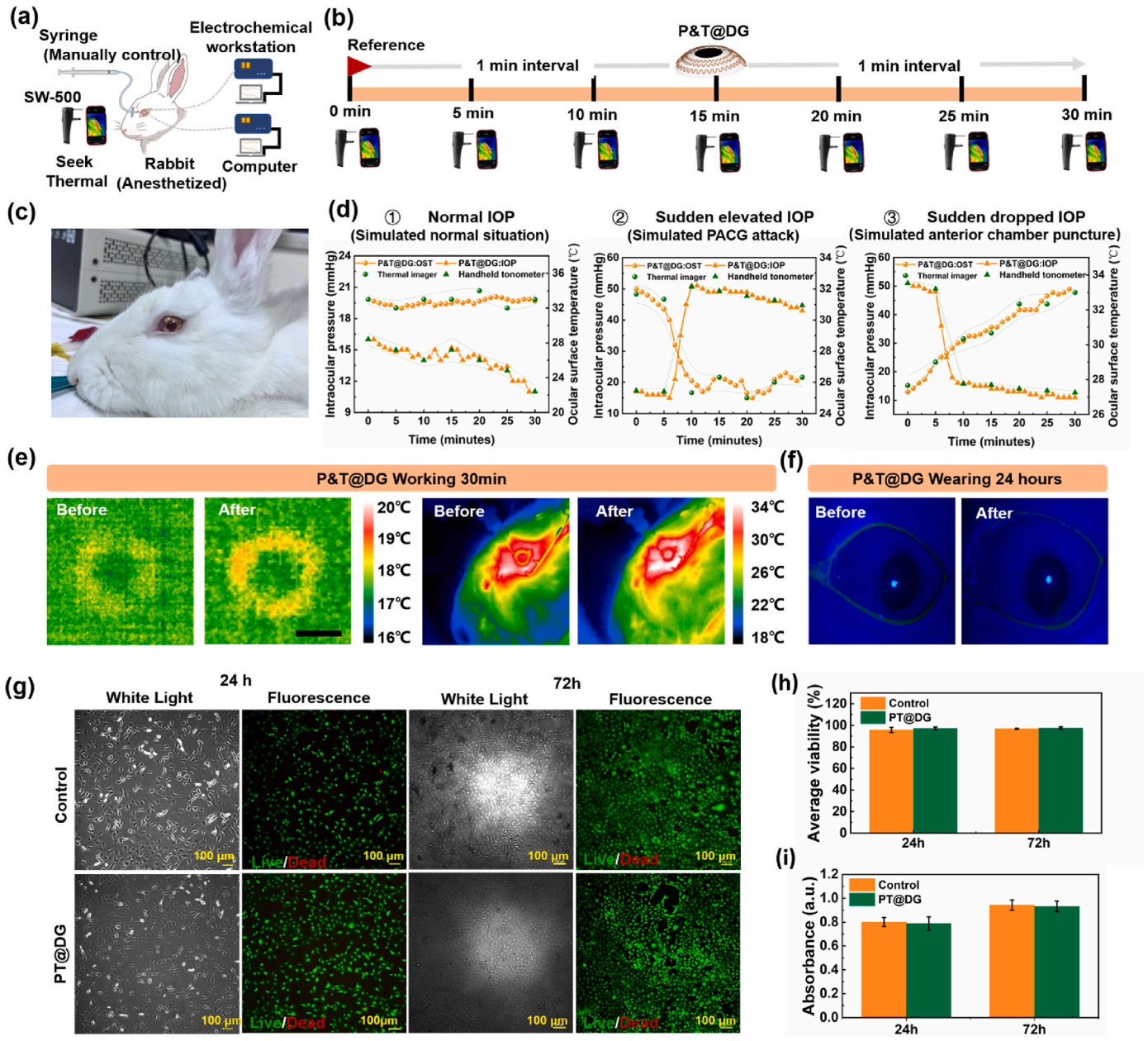

Fig. 4. Application of P&T@DG in rabbit eye *in vivo* and cell compatibility. (a) The sketch of the experimental platform. (b) The sketch of measurement time points. (c) Photograph of a rabbit wearing the *P&T @ DG*. (d) Representative captured values of IOP (orange line with triangles) and OST (orange line with dots) using *P&T @ DG*, compared with the results from the handheld tonometer (green triangles) and thermal imager (orange dots), under three different simulated fluctuation scenarios of normal situation, PACG attack, and anterior chamber puncture, respectively. (e) Heat generation test of a device using a thermal imager on a cardboard and a rabbit eyeball following a 30-min operational period. (f) Photographs rabbit cornea with sodium fluorescein staining under cobalt blue light slit lamp to detect the integrity of corneal epithelium for wearing *P&T @ DG* 24 h. (g) Photographs of the corneal epithelial cells using Live & dead cell staining method with(out) the device leaching liquid culturing for 24 and 72 h. (h) The average viability of corneal epithelial cells in two groups after the quantification of (g). Error bars correspond to the standard deviation for three measurements. (i) The absorbance of corneal epithelial cells using CCK8 experiment after the device leaching liquid culturing for 24 and 72 h, compared with the blank group. Error bars correspond to the standard deviation for three measurements. IOP: intraocular pressure.

inserted into the anterior chamber of the rabbit eye. This setup is utilized to replicate three distinct clinical scenarios: normal conditions, a major attack of primary angle closure glaucoma, and an anterior chamber puncture. These scenarios correspond to normal IOP, a sudden increase in IOP, and a sudden decrease in IOP, respectively. Fig. 4d exhibits the real-time measurement results of IOP (orange line with triangles) and OST (orange line with dots) via our *P&T@DG*, well consistent with the measured trends via handheld tonometer (green triangles) and thermal imager (orange dots). In all these cases, slight water leakage from the scalp needle inserted into the eyeball causes the downward trend of the measured IOP. Due to temperature interference with the fluid injected into the anterior chamber, the measured temperature value is not the exact OST.

To evaluate the potential hazard of heat generation by the device to animal models, a thermal imager examines the device following a 30-min operational period. After subjecting the device to operation positioned on both electrical cardboard and rabbit eyes for 30 min, the temperature of the device does not exhibit an increase exceeding 1 °C, indicating low heat generated by *P&T@DG* with bio-compatibility. Additionally, the OST of the rabbit does not surpass 34 °C, a value

within the established range for ocular surface, as depicted in Fig. 4e. These empirical findings provide evidence that the electronic device does not elicit thermal harm to the cornea.

Here, the bottom layer of PDMS, between the *P&T@DG* and ocular surface, can yield a soft, seamless intimate interface to targeted biological tissues, serving as a bio-integrated platform with high oxygen permeability (Dou et al., 2021; Fan et al., 2021; Guo et al., 2021; Liu et al., 2021; M Kouhani et al., 2020; Pang et al., 2019; Yang et al., 2022). The thickness of hundreds of microns in previous literature (Liu et al., 2020; M Kouhani et al., 2020; Mansouri and Weinreb, 2012) that is compatible with that of our fabricated devices (~360 μm) in Fig. S12, improves the oxygen flux and comfort for the use of the contact lens. Although it is hydrophobic, it can be modified into a hydrophilic surface by several methods, such as UV radiation, oxygen plasma treatment, and SiO_2 decoration (Li et al., 2023). Long-term wearing on living rabbit eyes for more than 1 day, without any epithelial damage (no obvious staining of epithelium) is shown in Fig. 4f. Proposed interface materials of hydrogels refer to composite materials, such as mixtures of hydroxyethylmethacrylate (HEMA) with other substances in varying ratios, although with higher comfort, are not suitable for the piezoresistive mechanism-based device due to its low modulus (~KPa), high water content, and relative lower oxygen permeability (Wang et al., 2020; Ye et al., 2022; Zare et al., 2021). Reduced mechanical stability and interface mismatch between the device and the ocular surface will induce uncertainty and mechanical sensing hysteresis for measurements in our case of Si-NR-based IOP gauge (~GPa level) (Kim et al., 2019; Liu et al., 2022; Tang et al., 2019). Compared to HEMA hydrogel, PDMS materials (~MPa level) can yield superior mechanical stability for our piezoresistive types of Si-NR-based IOP gauge, with minor viscoelastic effects under applied strain at low frequencies (Dagdeviren et al., 2015). Ongoing efforts seek smart materials for contact lenses that can optimize their characteristics such as oxygen permeability, wearing comfort to patients, and their bio-integration between functional devices and ocular surfaces.

For examination of the bio-compatibility of *P&T@DG* at the cellular scale, cell compatibility experiments appear in Fig. 4g–i by use of corneal epithelial cells that are the outermost cells of the cornea and are in contact with the device platform. The device is subjected to a 24-h leaching process, followed by co-culturing with corneal epithelial cells for 24 and 72 h. The results of immunofluorescence staining of live and dead cells, as depicted in Fig. 4g, indicate that there is no statistically significant disparity in average cell viability between the experimental and blank groups at each time point ($P > 0.05$) (Fig. 4h). Furthermore, the results of the CCK8 experiment demonstrate no significant differences in absorbance values between the experimental and control groups at each time point ($P > 0.05$) (Fig. 4i). By comparison between the control group and the group with *P&T@DG* application, Fig. 4h and i reveal that the average viability of corneal epithelial cells is almost at the same level. The aforementioned findings demonstrate the favorable compatibility of the device with corneal epithelial cells.

Furthermore, despite that *P&T@DG* provides powerful capabilities for precise, rapid evaluation of biomechanics and temperature of eye conditions, a critical challenge is that the system reported here involves benchtop readout detection electronics with wire connection. Our ongoing work focuses on the development of an integrated system to allow continuous monitoring of IOP and OST during daily life activities with a wireless remote-control design. A device design concept can address these requirements using adapted versions of wireless platforms used for other purposes (Yu et al., 2019). Briefly, the wireless platform forms a power module, a sensing module, and a process & transmit module. The IOP gauge and OST sensor form a sensing module and link to the signal processing module, comprising a bandpass filter (60 Hz) and amplifier (40 dB). Then processed sampling signals are transmitted to an analog-to-digital converter (ADC) to harvest the digital signal. A signal processing module and a microcontroller integrated with the Bluetooth technique configured into a flexible printed circuit board (FPCB), can replace the bulky detection electronics, while a wireless communication module can communicate with portable consumer electronic devices (i.e. a smartphone). Additional details appear in Fig. S13.

4. Conclusion

In conclusion, we successfully developed a multi-functional smart contact lens named *P&T@DG* with continuously accurate IOP fluctuation capturing and OST monitoring through a comprehensive experimental approach. The IOP gauge incorporates the large-scale Si-NR, resulting in a sensitivity of 0.03% $mmHg^{-1}$, enabling precise detection of IOP fluctuation both in the porcine eyeball *ex vivo* and rabbit eye *in vivo*. The OST sensor has been optimized for enhanced sensitivity to assist glaucoma diagnosis as well as calibrating the temperature shift of the IOP gauge. Compared to commercial devices and reported smart contact lenses, this smart contact lens offers several advantages, including assembly multi-functionality and continuously accurate measurements. Consequently, the construction of this contact lens holds immense significance in the clinical diagnosis of glaucoma and the evaluation of the therapeutic effects of glaucoma. Despite the huge potential, several challenges remain when applied to the clinical scene, including the wire-connection dependent, the signal disturbance due to eye blink and movement, and wearing discomfort for a long term. Ongoing efforts focus on the realization of a wireless platform with minimizing the PCB circuits or a soft chip, anti-interference design as well as improvement of the comfort for the long-term wear with a smart contact interface.

Data availability

The data are not publicly available due to their containing information that could compromise the privacy of research participants.

CRediT authorship contribution statement

Yuting Shao: Writing – original draft, Methodology, Investigation, Formal analysis, Data curation, Conceptualization. **Bofan Hu:** Methodology, Investigation. **Xin Liu:** Methodology, Formal analysis. **Zhuofan Ni:** Visualization, Formal analysis. **Yiyang Shu:** Resources, Formal analysis. **Xiruo Zhang:** Project administration. **Jiaqi Shen:** Project administration. **Li Liang:** Validation, Formal analysis. **Lianjie Zhou:** Writing – review & editing, Conceptualization. **Junhan Liu:** Investigation, Methodology, Software. **Xiao Li:** Writing – review & editing, Data curation. **Juan Zhang:** Project administration, Methodology. **Lichao Ma:** Writing – review & editing, Methodology. **Zengfeng Di:** Methodology, Writing – review & editing. **Yongfeng Mei:** Writing – review & editing, Resources, Methodology. **Rui Li:** Writing – review & editing, Visualization, Supervision, Resources, Project administration. **Yanlong Bi:** Writing – review & editing, Supervision, Resources, Project administration, Methodology, Conceptualization. **Enming Song:** Writing – review & editing, Writing – original draft, Visualization, Validation, Supervision, Resources, Project administration, Methodology, Investigation, Funding acquisition, Formal analysis, Data curation, Conceptualization.

Declaration of competing interest

Enming Song, Yanlong Bi, Yuting Shao, and Bofan Hu are inventors of a provisional patent application filed by Fudan University. The authors declare that they have no other competing financial interests or personal relationships that could have appeared to influence the work reported in this paper.

Data availability

Data will be made available on request.

Acknowledgment

This work is supported by the STI 2030-Major Project (2022ZD0209900), the National Natural Science Foundation of China (62204057, 62304044, 82070920, 12022209), Science and Technology Commission of Shanghai Municipality (22ZR1406400), State Key Laboratory of Integrated Chips and Systems (SKLICS-Z202306), Lingang Laboratory (LG-QS-202202-02) and we appreciate the support by the Clinical Research Project of Tongji Hospital of Tongji University (ITJ (ZD)2101), Guizhou Province Science and Technology Project (LC [2024]081), Shanghai Municipal Science and Technology Major Project (2018SHZDZX01), ZJ Lab, Shanghai Center for Brain Science and Brain-Inspired Technology, the young scientist project of MOE innovation platform, and the China Postdoctoral Science Foundation (2023M730712). (Part of) the sample fabrication was performed at the Fudan Nano-fabrication Laboratory (experimental work). Yuting Shao acknowledges the help from the teachers and friends from Fudan University, Dalian University of Technology, and Tongji University, the endless support from her husband and parents.

Appendix. ASupplementary data

Supplementary data to this article can be found online at https://doi.org/10.1016/j.bios.2024.116786.

References

Alstrup, A.K.O., Dollerup, M.R., Simonsen, M.I.T., Vendelbo, M.H., 2023. Semin. Nucl. Med. 53 (5), 570–576.
Baudouin, C., Kolko, M., Melik-Parsadaniantz, S., Messmer, E.M., 2021. Prog. Retin. Eye Res. 83, 100916.
Dagdeviren, C., Shi, Y., Joe, P., Ghaffari, R., Balooch, G., Usgaonkar, K., Gur, O., Tran, P. L., Crosby, J.R., Meyer, M., Su, Y., Chad Webb, R., Tedesco, A.S., Slepian, M.J., Huang, Y., Rogers, J.A., 2015. Nat. Mater. 14 (7), 728–736.
Dou, Z., Tang, J., Liu, Z., Sun, Q., Wang, Yang, Li, Y., Yuan, M., Wu, H., Wang, Yijun, Pei, W., Chen, H., 2021. Micromachines 12 (2), 108.
Fan, Y., Tu, H., Zhao, H., Wei, F., Yang, Y., Ren, T., 2021. Nanotechnology 32, 095106.
Gloe, S., Rothering, A., Kiland, J.A., McLellan, G.J., 2019. Exp. Eye Res. 185, 107698.
Guo, S., Wu, K., Li, C., Wang, H., Sun, Z., Xi, D., Zhang, S., Ding, W., Zaghloul, M.E., Wang, C., Castro, F.A., Yang, D., Zhao, Y., 2021. Matter 4 (3), 969–985.
Jayaram, H., Kolko, M., Friedman, D.S., Gazzard, G., 2023. Lancet Lond. Engl. 402 (10414), 1788–1801.
Kanda, Y., 1991. Sens. ACTUATORS -Phys. 28 (2), 83–91.
Kim, J., Kim, M., Lee, M.S., Kim, K., Ji, S., Kim, Y.T., Park, J., Na, K., Bae, K.H., Kyun Kim, H., Bien, F., Young Lee, C., Park, J.U., 2017. Nat. Commun. 8, 14997.
Kim, J., Lee, M., Shim, H.J., Ghaffari, R., Cho, H.R., Son, D., Jung, Y.H., Soh, M., Choi, C., Jung, S., Chu, K., Jeon, D., Lee, S.T., Kim, J.H., Choi, S.H., Hyeon, T., Kim, D.H., 2014. Nat. Commun. 5, 5747.
Kim, Joohee, Park, J., Park, Y.G., Cha, E., Ku, M., An, H.S., Lee, K.P., Huh, M.I., Kim, Junmo, Kim, T.S., Kim, D.W., Kim, H.K., Park, J.U., 2021. Nat. Biomed. Eng. 5 (7), 772–782.
Kim, Y.W., Kim, J.E., Jung, Y., Sun, J.Y., 2019. Mater. Sci. Eng. C Mater. Biol. Appl. 95, 86–94.
Lee, C.H., Kim, D.R., Zheng, X., 2011. Nano Lett. 11 (8), 3435–3439.
Lee, P.P., Sultan, M.B., Grunden, J.W., Cioffi, G.A., 2010. IOP consensus panel. J. Glaucoma 19 (5), 281–287.
Leidl, M.C., Choi, C.J., Syed, Z.A., Melki, S.A., 2014. Br. J. Ophthalmol. 98 (10), 1315–1319.
Leonardi, M., Pitchon, E.M., Bertsch, A., Renaud, P., Mermoud, A., 2009. Acta Ophthalmol. 87 (4), 433–437.
Leshno, A., Stern, O., Barkana, Y., Kapelushnik, N., Singer, R., Prat, D.L., Cohen, G., Ben-David, G., Abrahami, D., Huna-Baron, R., Skaat, A., 2022. Eur. J. Ophthalmol. 32 (3), 1518–1524.
Li, S., Zhang, J., He, J., Liu, W., Wang, Y., Huang, Z., Pang, H., Chen, Y., 2023. Adv. Sci. Weinh. Baden-Wurtt. Ger. 10 (34), e2304506.
Liu, J.H.K., Zhang, X., Kripke, D.F., Weinreb, R.N., 2003. Invest. Ophthalmol. Vis. Sci. 44 (4), 1586–1590.
Liu, S., Rao, Y., Jang, H., Tan, P., Lu, N., 2022. Matter 5 (4), 1104–1136.
Liu, X., Ye, Y., Ge, Y., Qu, J., Liedberg, B., Zhang, Q., Wang, Y., 2024. ACS Nano 18 (9), 6817–6844.
Liu, Z., Wang, G., Pei, W., Wei, C., Wu, X., Dou, Z., Li, Y., Wang, Y., Chen, H., 2020. J. Mater. Chem. B 8 (38), 8794–8802.
Liu, Z., Wang, G., Ye, C., Sun, H., Pei, W., Wei, C., Dai, W., Dou, Z., Sun, Q., Lin, C.T., Wang, Y., Chen, H., Shen, G., 2021. Adv. Funct. Mater. 31 (29), 2010991.
M Kouhani, M.H., Wu, J., Tavakoli, A., Weber, A.J., Li, W., 2020. Lab Chip 20 (2), 332–342.
Mansouri, K., Weinreb, R.N., 2012. Expert Rev. Med. Devices 9 (3), 225–231.
Medeiros, F.A., Weinreb, R.N., Zangwill, L.M., Alencar, L.M., Sample, P.A., Vasile, C., Bowd, C., 2008. Ophthalmology 115 (6), 934–940.
Nambiar, M.H., Liechti, L., Muller, F., Bernau, W., Studer, H., Roy, A.S., Seiler, T.G., Buchler, P., 2022. Exp. Eye Res. 224, 109266.
Pang, Y., Li, Y., Wang, X., Qi, C., Yang, Y., Ren, T.L., 2019. RSC Adv. 9 (9), 5076–5082.
Qiu, Y., Yang, H., Lei, B., 2014. Curr. Eye Res. 39 (4), 365–369.
Ray, T.R., Choi, J., Bandodkar, A.J., Krishnan, S., Gutruf, P., Tian, L., Ghaffari, R., Rogers, J.A., 2019. Chem. Rev. 119 (8), 5461–5533.
Shen, Y., Lifante, J., Zabala-Gutierrez, I., de la Fuente-Fernández, M., Granado, M., Fernández, N., Rubio-Retama, J., Jaque, D., Marin, R., Ximendes, E., Benayas, A., 2022. Adv. Mater. Deerfield Beach Fla 34 (7), e2107764.
Shi, Y., Jiang, N., Bikkannavar, P., Cordeiro, M.F., Yetisen, A.K., 2021. The Analyst 146 (21), 6416–6444.
Shih, H.J., Cheng, S.C., Shih, P.J., 2024. J. Mech. Behav. Biomed. Mater. 152, 106454.
Shin, D.Y., Park, H.Y.L., Shin, H., Oh, S.E., Kim, S.A., Jung, Y., Lee, M.Y., Park, C.K., 2023. Am. J. Ophthalmol. 254, 69–79.
Sihota, R., Angmo, D., Ramaswamy, D., Dada, T., 2018. Indian J. Ophthalmol. 66 (4), 495–505.
Son, D., Lee, J., Qiao, S., Ghaffari, R., Kim, J., Lee, J.E., Song, C., Kim, S.J., Lee, D.J., Jun, S.W., Yang, S., Park, M., Shin, J., Do, K., Lee, M., Kang, K., Hwang, C.S., Lu, N., Hyeon, T., Kim, D.H., 2014. Nat. Nanotechnol. 9 (5), 397–404.
Subramaniam, A.G., Allen, P., Toh, T., 2021. Ophthalmic Res. 64 (2), 321–326.
Tan, J.H., Ng, E.Y.K., Acharya, U.R., Chee, C., 2009. Infrared Phys. Technol. 52 (4), 97–108.
Tan, L., Cai, Z.Q., Lai, N.S., 2009. Contact lens anterior eye J. Br. Contact Lens Assoc 32 (2), 78–83.
Tang, J., Yin, Q., Qiao, Y., Wang, T., 2019. ACS Appl. Mater. Interfaces 11 (23), 21194–21200.
Tham, Y.C., Li, X., Wong, T.Y., Quigley, H.A., Aung, T., Cheng, C.Y., 2014. Ophthalmology 121 (11), 2081–2090.
Turner, D.C., Edmiston, A.M., Zohner, Y.E., Byrne, K.J., Seigfreid, W.P., Girkin, C.A., Morris, J.S., Downs, J.C., 2019. Invest. Ophthalmol. Vis. Sci. 60 (7), 2572–2582.
Vitish-Sharma, P., Acheson, A.G., Stead, R., Sharp, J., Abbas, A., Hovan, M., Maxwell-Armstrong, C., Guo, B., King, A.J., 2018. Acta Ophthalmol. 96 (2), e242–e246.
Wang, Y., Zhao, Q., Du, X., 2020. J. Mater. Chem. B 8 (16), 3519–3526.
Weinreb, R.N., Aung, T., Medeiros, F.A., 2014. JAMA 311 (18), 1901–1911.
Xu, J., Cui, T., Hirtz, T., Qiao, Y., Li, X., Zhong, F., Han, X., Yang, Y., Zhang, S., Ren, T.L., 2020. ACS Appl. Mater. Interfaces 12 (16), 18375–18384.
Yang, Cheng, Huang, X., Li, X., Yang, Chengduan, Zhang, T., Wu, Q., Liu, D., Lin, H., Chen, W., Hu, N., Xie, X., 2021. Adv. Sci. Weinh. Baden-Wurtt. Ger. 8 (6), 2002971.
Yang, Cheng, Wu, Q., Liu, J., Mo, J., Li, X., Yang, Chengduan, Liu, Z., Yang, J., Jiang, L., Chen, W., Chen, H.J., Wang, J., Xie, X., 2022. Nat. Commun. 13 (1), 2556.
Yang, H., Zhu, H., Liu, H., Mao, Z., Luo, J., Zhu, S., Hu, Z., Yuan, S., Xu, F., 2024. Adv. Funct. Mater. https://doi.org/10.1002/adfm.202400722.
Yang, S., Lu, N., 2013. Sensors 13 (7), 8577–8594.
Ye, Y., Ge, Y., Zhang, Q., Yuan, M., Cai, Y., Li, K., Li, Y., Xie, R., Xu, C., Jiang, D., Qu, J., Liu, X., Wang, Y., 2022. Adv. Sci. Weinh. Baden-Wurtt. Ger. 9 (12), e2104738.
Yu, X., Xie, Z., Yu, Yang, Lee, J., Vazquez-Guardado, A., Luan, H., Ruban, J., Ning, X., Akhtar, A., Li, D., Ji, B., Liu, Y., Sun, R., Cao, J., Huo, Q., Zhong, Y., Lee, C., Kim, S., Gutruf, P., Zhang, C., Xue, Y., Guo, Q., Chempakasseril, A., Tian, P., Lu, W., Jeong, J., Yu, YongJoon, Cornman, J., Tan, C., Kim, B., Lee, K., Feng, X., Huang, Y., Rogers, J.A., 2019. Nature 575 (7783), 473–479.
Zare, Mina, Bigham, A., Zare, Mohamad, Luo, H., Ghomi, E.R., Ramakrishna, S., 2021. Int. J. Mol. Sci. 22 (12), 6376.
Zhu, H., Yang, H., Zhan, L., Chen, Y., Wang, J., Xu, F., 2022. ACS Sens. 7 (10), 3014–3022.
Zhu, Y., Li, S., Li, J., Falcone, N., Cui, Q., Shah, S., Hartel, M.C., Yu, N., Young, P., de Barros, N.R., Wu, Z., Haghniaz, R., Ermis, M., Wang, C., Kang, H., Lee, J., Karamikamkar, S., Ahadian, S., Jucaud, V., Dokmeci, M.R., Kim, H.J., Khademhosseini, A., 2022. Adv. Mater. Deerfield Beach Fla 34 (24), e2108389.